research papers

Precession electron diffraction 1: multislice simulation

C. S. Own,[a]* L. D. Marks[a] and W. Sinkler[b]

[a]Department of Materials Science and Engineering, Northwestern University, Evanston, IL 60208, USA, and [b]UOP LLC, Des Plaines, IL 60208, USA. Correspondence e-mail: csown@northwestern.edu

Precession electron diffraction (PED) is a method that considerably reduces dynamical effects in electron diffraction data, potentially enabling more straightforward solution of structures using the transmission electron microscope. This study focuses upon the characterization of PED data in an effort to improve the understanding of how experimental parameters affect it in order to predict favorable conditions. A method for generating simulated PED data by the multislice method is presented and tested. Data simulated for a wide range of experimental parameters are analyzed and compared to experimental data for the $(Ga,In)_2SnO_4$ (GITO) and ZSM-5 zeolite (MFI) systems. Intensity deviations between normalized simulated and kinematical data sets, which are bipolar for dynamical diffraction data, become unipolar for PED data. Three-dimensional difference plots between PED and kinematical data sets show that PED data are most kinematical for small thicknesses, and as thickness increases deviations are minimized by increasing the precession cone semi-angle ϕ. Lorentz geometry and multibeam dynamical effects explain why the largest deviations cluster about the transmitted beam, and one-dimensional diffraction is pointed out as a strong mechanism for deviation along systematic rows. R factors for the experimental data sets are calculated, demonstrating that PED data are less sensitive to thickness variation. This error metric was also used to determine the experimental specimen thickness. R_1 (unrefined) was found to be about 12 and 15% for GITO and MFI, respectively.

1. Introduction

Rapid structural analysis of novel crystal phases is of large importance to a number of industrial and academic fields, for example in zeolite synthesis for adsorbents and catalysts, in compound semiconductor development, and in biomaterials. Knowledge of the crystal structure is critical in such fields because it is needed in order to assess the potential of any new compound. The need for tools that can rapidly provide reliable indications of crystal structure (for example without needing to grow large single crystals) has increased as high-throughput synthesis techniques provide ever more efficient means for systematic discovery of novel compounds. The family of diffraction techniques for directly recovering structure maps from diffraction intensities, direct methods (DM), provides structure information in the picometre regime. To recover atom positions accurately, conventional direct methods require that the intensities be primarily kinematical, *e.g.* the result of single scattering events. X-ray techniques have historically been the primary method for obtaining kinematical diffraction intensities for crystallographic studies, however, as the length scale of interest in materials investigations has steadily decreased, methods capable of forming

fine probes to obtain local structural information from 0.1–10 nm regions are in greater demand. The transmission electron microscope (TEM) is one machine that can do this, finding critical use in several types of nanoscale studies due to fine probe capabilities and a variety of characterization techniques simultaneously available within one (relatively inexpensive) machine.

While TEM has been very effective in studying atomic scale phenomena at surfaces and interfaces, investigations of the bulk have in general been hindered by multiple scattering due to the strong interaction of electrons with matter. For instance, in the presence of a screw axis or a glide plane, diffraction spots that are forbidden in X-ray diffraction are in general allowed in dynamical diffraction, the classic Gjønnes–Moodie lines (Gjønnes & Moodie, 1965). As a consequence, determining these symmetry elements from a spot diffraction pattern is often dangerous to impossible.

An electron diffraction technique that has recently garnered considerable interest, precession electron diffraction (PED), has been a promising development in diffraction-based crystallographic methods because it reduces the severity of the dynamical diffraction problem in the TEM. The method involves conically rocking the illuminating electron beam,

sequentially tracing out a path of tilts that avoid exciting the zone-axis condition (Fig. 1). The diffracted intensities are then de-scanned in a complementary fashion to bring the deflected beams to the location on the collection medium where the equivalent on-zone (non-tilted) spots would be.

The improved quality of the precession data over that of conventional ED has been demonstrated experimentally (Vincent & Midgley, 1994; Own *et al.*, 2004), and a small number of structures have been solved *via* the technique, some *a priori* (Gjønnes, Hansen *et al.*, 1998; Gemmi *et al.*, 2003; Own *et al.*, 2006a; Weirich *et al.*, 2006) and others by a combination of simulation and/or correction using forward calculations from known structure factors (Vincent & Midgley, 1994;

Gjønnes, Cheng *et al.*, 1998). Additionally, precession has been used to derive Debye–Waller temperature factors from monoatomic specimens using Wilson plots with good accuracy (Midgley *et al.*, 1998). Two recent studies involving *a priori* solution of PED data collected from oxide materials have been encouraging because they show straightforward solution of complex structures without substantial data processing or previously known crystallographic phases (Own *et al.*, 2006a; Weirich *et al.*, 2006). One other significant advantage of PED is that in many cases reflections that are kinematically forbidden due to a glide plane or screw axis have very low intensity in the PED pattern, so symmetry determination becomes much simpler.

While promising, *a priori* structure determination of unknown or partially known material phases using PED has met with varied success, primarily because a rigorous understanding of the deviations from kinematical structure factors has not been established. Precession data have been simulated only once previously in an investigation of a thick crystal (Al$_m$Fe, with nominal thickness 150 nm), where dynamical
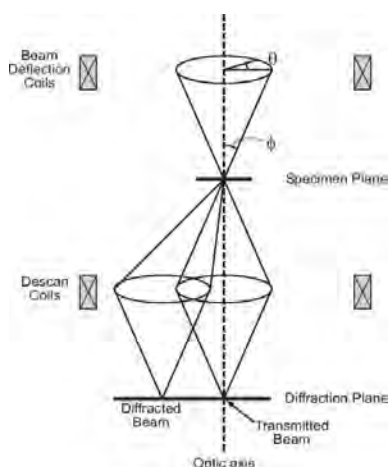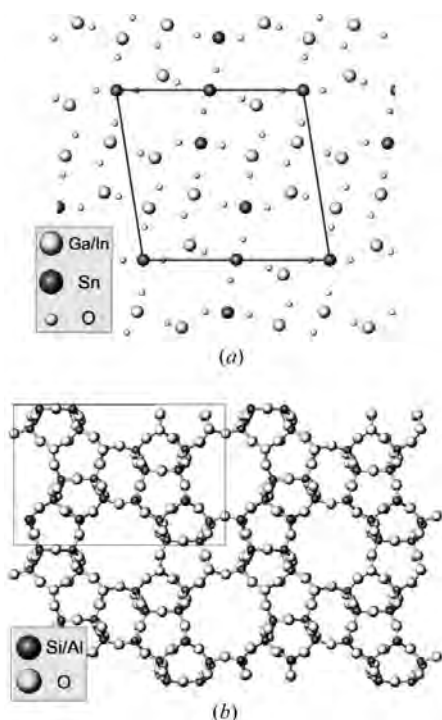

Figure 1
Simplified schematic of precession geometry.

Figure 2
Structure maps of the [010] projections of (*a*) GITO and (*b*) MFI.
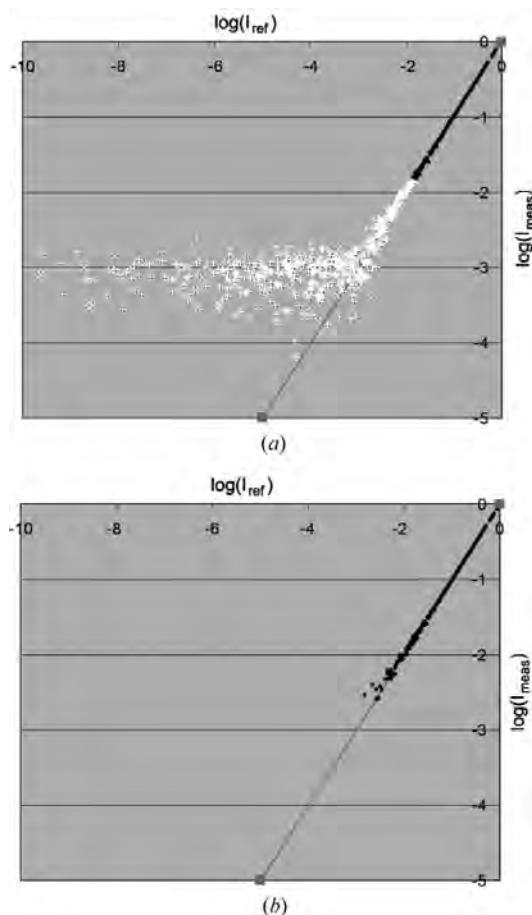

Figure 3
(*a*) Semper-measured Gaussian intensity profiles. The straight line corresponds to the true spot intensities. Lighter data points correspond to low-intensity spots and spots below the measurement floor. (*b*) EDM-measured intensity profiles. The cut-off is just above the noise floor measured by Semper, with good correspondence to the true intensity over 2.5 orders of magnitude.

intensities starting from a small accurate set of starting structure factors were corrected using structure factors from key systematic rows determined through careful CBED measurements and *n*-beam simulation (Cheng *et al.*, 1996; Gjønnes, Cheng *et al.*, 1998). Bloch *n*-beam calculations were made along the azimuthal precession circuit θ within $0.5°$ of the Bragg condition for each reflection and were reported to converge using a small number of beams within an aperture radius of 1 Å^{-1} (roughly 20 beams, varying in quantity and selection with Bragg reflection along the circuit) (Gjønnes, Cheng *et al.*, 1998). Details of which beams were used, how they were chosen, and the resolution of the calculation were unfortunately never published.

This paper is the first of a two-part analysis of PED data, primarily forward calculations *via* a multislice approach but we will also include a comparison to experimental data. In this paper, we focus on a comparison of PED results with kinematical intensities; in the discussion we analyze what the consequences of this are for a direct-methods analysis. The second part of this series (Own *et al.*, 2006*b*) will focus upon the simplest approximation to multiple scattering, the two-beam model, and establish some groundwork on which to base more sophisticated predictive methods.

2. Materials and methods

The two structures simulated were the [010] zone of GITO and the [010] zone of MFI. Structure representations for the relevant projections are given in Fig. 2. Experimental precession data sets were collected for direct comparisons with the calculations. Numerical values for the experimental intensities are given in Tables 1 and 2.[1]

2.1. Experimental

The GITO *m*6 phase has a monoclinic unit cell (plane group *p*2) with $a = 11.69$, $b = 3.17$, $c = 10.73 \text{ Å}$ and $\beta = 99°$. Its structure was determined by electron diffraction and high-resolution TEM and was later confirmed by neutron diffraction (Sinkler, Marks *et al.*, 1998; Edwards *et al.*, 2000). The heavy elements in the structure make it a strong dynamical scatterer, which projects well for the zone axis investigated here ([010]). The GITO specimen came from the same sample used in the studies referenced above.

MFI, also known as ZSM-5, is an industrially important large-pore zeolite. Its structure is orthorhombic (space group *Pnma*) with cell dimensions $a = 20.1$, $b = 19.9$, $c = 13.4 \text{ Å}$, and in the [010] zone axis projection the plane group is *p*2*gg*. For MFI, the published structure was used (Olson *et al.*, 1981). The specimen was prepared in ion-exchanged and calcined (acid) form, so there were essentially no cations in the pores except for H^+. The crystal size was approximately 350 nm along [010] and XRD confirmed the structure to be orthorhombic. The Si:Al ratio was approximately 22:1, therefore random substi-

tution of cations will not affect the results in an *a priori* structure study.

Experimental precession data were collected on JEOL 2000FX and JEOL 3000F microscopes retrofitted with a second-generation precession system developed at Northwestern University (Own *et al.*, 2005). Parallel illumination in nanobeam diffraction mode (10 µm condenser aperture) minimized the convergence and sampled area (~50 nm); also, for GITO we used 200 kV and a range of tilt angles whereas for MFI 300 kV and a 33 mrad semi-angle were used. For reference, non-precessed patterns were also taken from the same specimen region using identical exposure times and illumination conditions except the beam precession. Refer to Own *et al.* (2006*a*) for the detailed data-collection procedure on the 2000FX. MFI data sets were captured using the same collection medium (a Gatan US1000 CCD camera) on the 3000F.

Intensity values were measured from a single digital image for each data set using two methods. One method used EDM software (Kilaas *et al.*, 2005), which uses a composite of several reflection profiles (unitary spot motif) to find and quantify diffraction spots *via* cross-correlation. The algorithm is based upon the second method, a measurement script written in Semper (Saxton *et al.*, 1979) and described in Xu *et al.* (1994). The GITO data sets were measured by EDM, and MFI data sets were measured using Semper. Consistency between these two measurement methods was confirmed by measuring a
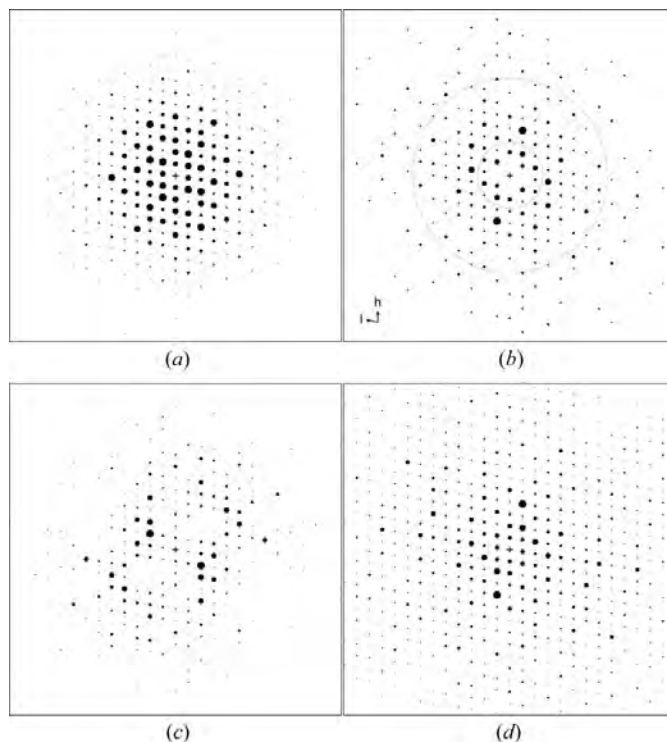

Figure 4
Diffraction patterns for GITO: (*a*) and (*b*) are experimental conventional diffraction and precession diffraction patterns, respectively. (*c*) Simulated on-zone conventional diffraction pattern and (*d*) simulated precession diffraction pattern for $t = 41.5$ nm. An annulus describing the range 0.25–0.75 Å^{-1} is bounded by the circles. The areas of the diffraction spots are proportional to the intensity.

---

[1] Tables 1 and 2 are available from the IUCr electronic archives (Reference: WE5013). Services for accessing these tables are described at the back of the journal.

simulated diffraction data set – a high-resolution 8-bit image of periodic Gaussian-shaped intensities ranging over 10 orders of magnitude – using both methods. Semper was more sensitive, being able to extract almost three orders of magnitude from the 8-bit image by virtue of intrinsic subpixel manipulation, while EDM reliably extracted intensities over 2.5 orders of magnitude and coincided with the Semper results almost exactly over EDM's measured range (Fig. 3). The experimental diffraction patterns for precessed and non-precessed patterns are given in Figs. 4(a)–(b) for GITO and Figs. 5(a)–(b) for MFI.

2.2. Numerical method

Precession diffraction simulations involve forward calculation of the diffracted intensities for a range of incident directions, then a (incoherent) summation of the intensities. For higher-order Laue-zone (HOLZ) data, a Bloch-wave method is preferred, since multislice in general does a poor job with these. Our approach has been to use a 'conventional' multislice approach (e.g. Ma & Marks, 1990), although we note that the method of Ishizuka (1982) might be more appropriate particularly for thicker samples.

Individual tilts were calculated with a fixed cone semi-angle (ϕ) and the intensities summed. Fig. 6 is an example of one tilt element within the summation. It was assumed that incident-beam convergence was negligible (i.e. only tilts lying exactly on the precession cone were used). Each separate incident-beam direction was a single multislice calculation, and at appropriate thicknesses the intensities were added to a cumulative array, and the code was slightly modified to enable a loop over a large number of incident directions. To minimize artifacts, the reciprocal-space sampling was set by requiring that >99.5% of incident intensity was retained for all simulations to 160 nm, which in practice was sampling to about 7.5 Å^{-1}. The output included reflections to 1.5 Å^{-1}, just beyond the measurement limit for most experimental data sets which do not include HOLZ reflections. For non-precessed data, the same conditions were used for consistency. No imaginary terms (optical potential) were included in the potential.

Simulation parameters were closely matched to the experimental conditions to allow a direct comparison. While illumination conditions, apertures and energies are easily duplicated, specimen thickness uniformity is not easy to control or characterize in situ, so regions appearing to be fairly uniform (minimal thickness fringes) and thin were selected during the experiment. The simulations for GITO used a slice thickness of $c/2$ (1.59 Å) with neutron-refined atom positions and isotropic temperature factors given in the literature (Edwards et al., 2000). MFI simulations used a slice thickness of 1.99 Å and used literature Debye–Waller factors (Olson et al., 1981).

A critical parameter is the granularity of the simulation (azimuthal angular resolution) which can be written as $360°/N$ with units of degrees, where N is the number of discrete tilts. The numerical convergence is a function of N that we quantify
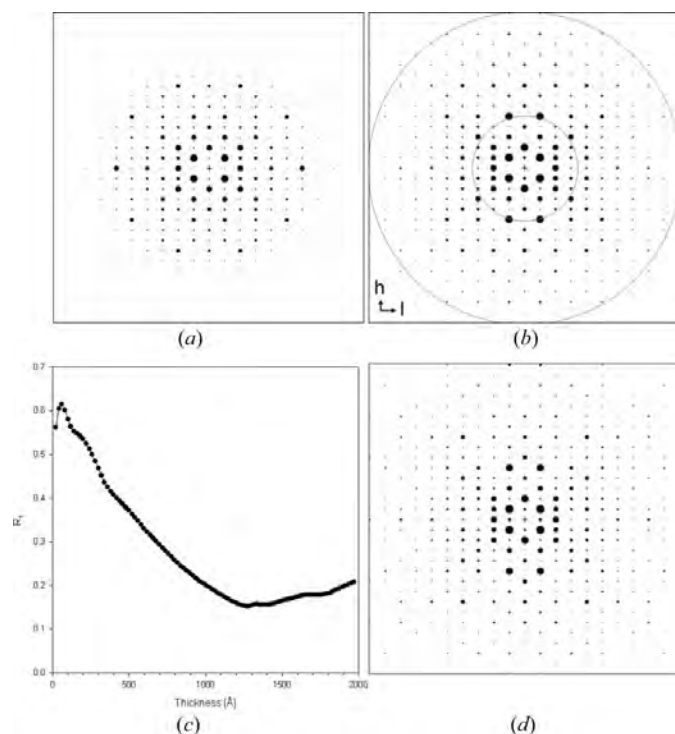

Figure 5
(a) The experimental intensities (non-precessed) and (b) experimental precession intensities. (c) R_1 for the MFI experimental precession data set. Multislice done at 33 mrad, 2048 points, 300 kV. (d) shows the multislice calculation with the lowest R factor of 15.26% at 127.3 nm. Note that many strong reflections with ordering are present near the transmitted beam, falling outside the annulus describing reciprocal distances of 0.25 to 0.75 Å^{-1}. The areas of the diffraction spots are proportional to the intensity.

Figure 6
One diffraction pattern from the series of patterns that were summed in the precession multislice code for GITO at an azimuthal angle of $\pi/2$ and a cone semi-angle of 24 mrad. A close to systematic row condition is excited along the **l** direction for this tilt. The diffraction spot areas are proportional to intensity

using R factors parameterized in terms of the largest value used ($N_{max} = 1000$ for GITO and $N_{max} = 2048$ for MFI):

$$R_2(N, t, \phi) = \frac{\sum_g |I_g^{N_{max},t,\phi} - I_g^{N,t,\phi}|}{\sum_g |I_g^{N_{max},t,\phi}|}, \quad (1)$$

where $I_g^{N,t,\phi}$ and $I_g^{N_{max},t,\phi}$ are calculated intensities for N discrete tilts and for the maximum granularity, respectively (for a given thickness and tilt), as functions of the cone semi-angle ϕ for different reciprocal-lattice vectors $\mathbf{g}$. Convergence results are shown in Fig. 7. The simulated data sets were normalized to incident amplitude by dividing intensities by N. It was found that convergence for small thicknesses was rapid (Fig. 7a), however, at larger thicknesses and angles, much higher resolution was necessary for convergence. Fig. 7(b) demonstrates that thickness is more limiting for simulation convergence than cone angle. Because reciprocal space is sampled more sparsely with increasing tilt and the intensity oscillations as a function of incident-beam direction increase
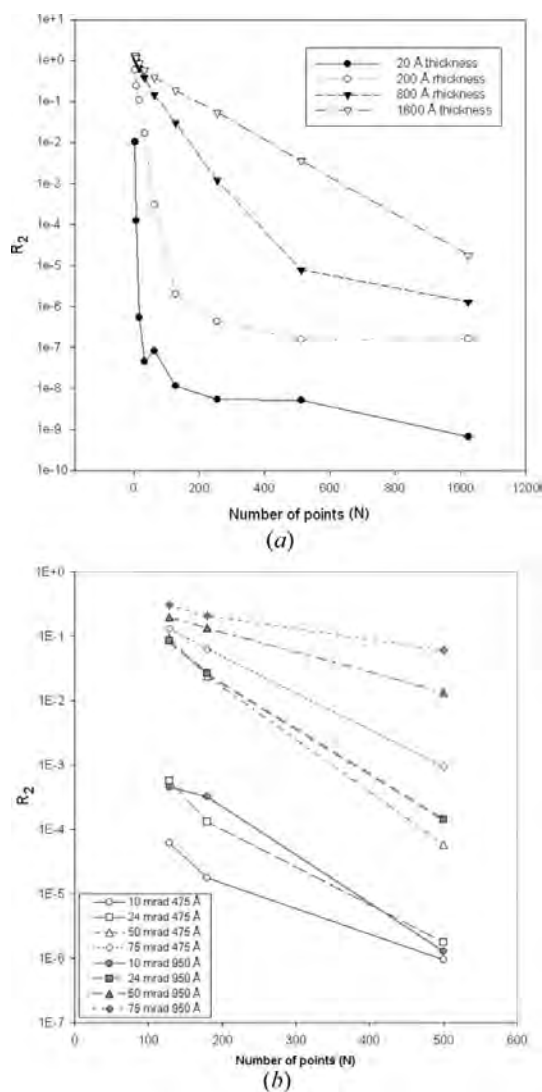

Figure 7
Convergence of the precession multislice using (a) MFI zeolite [010] projection for cone semi-angle of 36 mrad as a function of thickness, and (b) GITO [010] with varied cone semi-angles and thicknesses.

with thickness, simulation of large thickness crystals using a large precession angle requires very fine sampling. In the following analyses on GITO, the largest error between 500 and 1000 sampling points is $R_2 = 0.125$, occurring for $\phi = 75$ mrad and $t = 1580$ Å.

3. Results

A numerical multislice (or Bloch-wave) calculation gives 'correct' results but says very little about the general character of the results; the latter is critical to understanding PED and knowing when it may (or may not) be a viable technique for solving a structure. One metric is to plot the simulation results against kinematical intensities. To eliminate scaling issues, in all subsequent comparisons we arbitrarily normalized the strongest intensity to unity.

A montage of reference plots of multislice precession data for GITO is given in Fig. 8 demonstrating trends over a wide range of thickness t and cone semi-angle ϕ. The montage is divided into three data-set groups:

1. The top row of plots is the un-precessed case (dynamical).

2. The left column shows the behavior for a very thin specimen (4 nm).

3. The block of 16 plots at lower right show the effect of increasing precession angle for a variety of specimen thicknesses.

The precession angle ϕ of 10, 24, 50 and 75 mrad corresponds to reciprocal distances (in Å^{-1}) of 0.398, 0.956, 1.99 and 2.99, respectively, at 200 kV. Note that, even for 4 nm thickness, the conventional data are not well described as kinematical, as expected for a material with well projecting heavy atoms. A qualitative analysis of the precession multislice data reveals interesting global behaviors. As would be expected, the data become less kinematical with increasing t regardless of precession angle, but how rapidly this occurs depends upon the cone semi-angle and, in general, the larger the cone angle, the more kinematical are the results, provided that the thickness is not too large. Deviation from kinematical occurs primarily in the weak reflections, where precession tends to create a positive offset; previously (Own *et al.*, 2006a), we pointed out that the affected reflections were most commonly found near the transmitted beam because this is where the precession only scans over a limited range of excitation error. This overemphasis of weak beams is reduced for a given thickness when the precession angle is increased.

An alternative approach is to analyze the absolute deviations E_{norm} of the normalized precession multislice data sets from kinematical $E_{norm} = |F_g^{exp}| - |F_g^{kin}|$, where F_g^{exp} and F_g^{kin} are the experimental and kinematical structure factors, as a three-dimensional surface, plotted with respect to $|\mathbf{g}|$ and thickness t (Fig. 9, for GITO). These 'lobster tail' plots give a wide view of experiment space within a single plot. To be able to describe the data as kinematical, one wants small deviation throughout the data set, although, for reasons that we will return to later, the 'structure-defining reflections' that lie within the range 0.25–1.0 Å^{-1} are the most important ones. This range contains the spatial frequencies that, when

inverted, reconstruct the key structural features that describe distances between peaks and define their locations (Sinkler, Marks *et al.*, 1998; Sinkler, Bengu & Marks, 1998). Fig. 9 is subdivided into blocks corresponding to 20% amplitude difference. The regime of most interest is the band corresponding to ±0.4 (blue/dark blue).

Fig. 9(*a*) is the difference surface for the non-precessed diffraction data set plotted with respect to **g** and *t*. The surface demonstrates the classic damping effect where reflections near the transmitted beam are strong and their amplitudes decay with **g** (*e.g.*, when intensities are large, their distortion will probably be large as well). For small *t*, there is substantial deviation beyond the ±40% range indicating strong dynamical effects. Oscillations are relatively high in amplitude, though most differences are on the order of about 0.2–0.4. The important structure-defining reflections are the most adversely affected, with amplitude deviation as high as ~0.6, and demonstrate rapid oscillatory behavior as *t* increases.

Introducing PED at 10 mrad (Fig. 9*b*) reduces the maximum deviation to <0.8 and the difference surface is flattened. More notably, most negative deviations are eliminated. Gaussian radial damping is still present for all thicknesses, and 10 mrad is still quite dynamical even for small thickness where dynamical effects should be lowest, in accordance with the 10 mrad plots in Fig. 8. Increasing the angle to 24 mrad enhances the flattening effect considerably, and the data from thin crystals becomes nearly kinematical (Fig. 9*c*). As the thickness increases, the deviations from kinematical grow, especially for small **g**. The peak occurs for the largest thickness (160 nm) near the transmitted beam. A large precession semi-angle (Figs. 9*d*–*e*) decreases the overall deviation and additionally flattens the small-thickness region like a serrated knife-edge such that intensities remain kinematical for larger thickness (~5 nm more for each 25 mrad step in angle). Fig. 9(*f*) is a scatter plot for ϕ = 24 mrad that shows that the error surface is thin (low oscillation) and is sharply tilted up toward
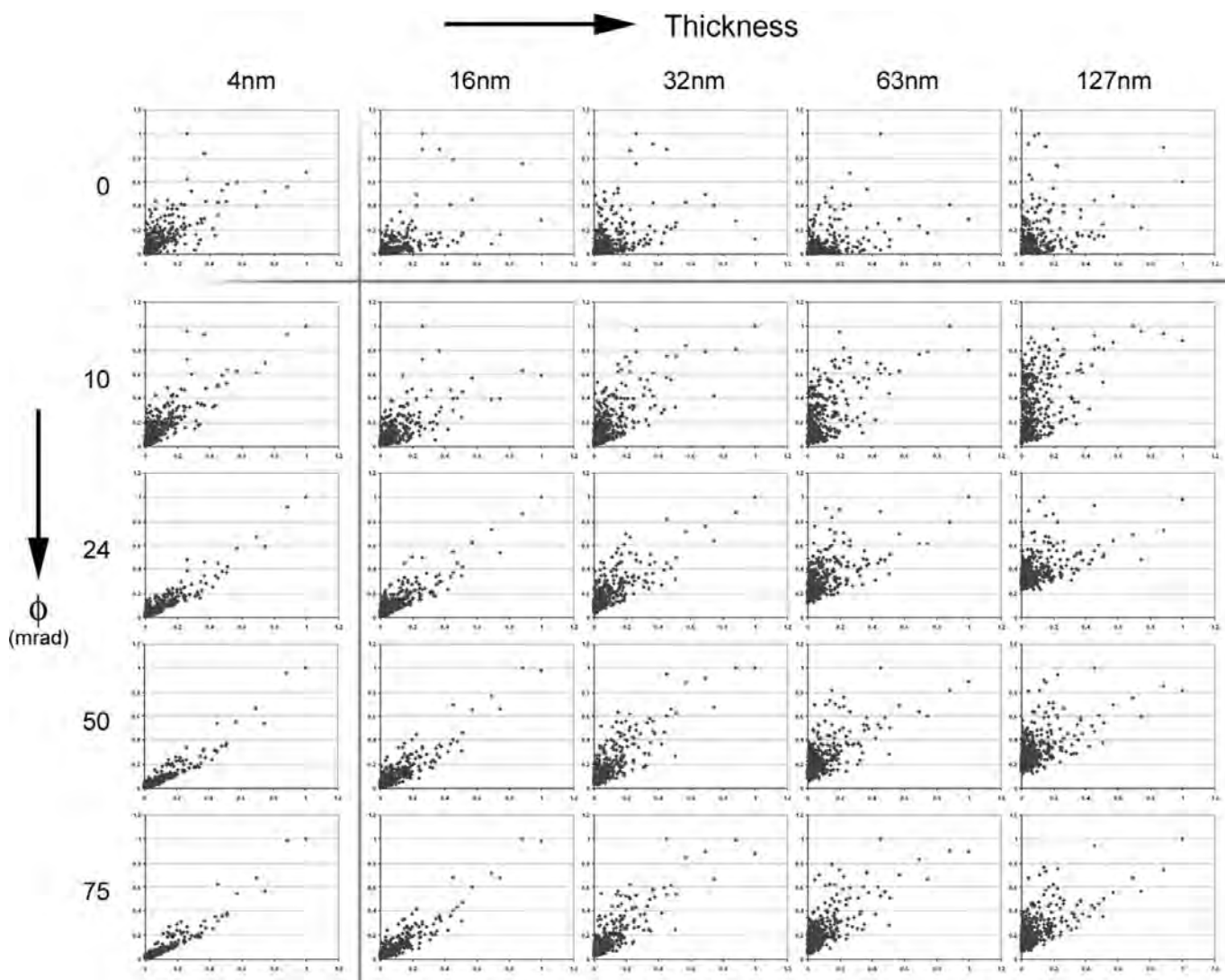

Figure 8
Montage of amplitude reference plots for GITO. In each plot, the abscissa represents the absolute value of the kinematical amplitudes and the absolute value of the calculated amplitudes are plotted along the ordinate. The plots are arranged in order of increasing thickness and angle as indicated.

small **g** and very large t. This is common for all precession data sets above 20 mrad precession angle.

The final result we will show is a comparison against experimental data. To eliminate scaling issues, in all subsequent comparisons we arbitrarily normalized the strongest intensity to unity. We used a conventional R factor, treating the atom positions as fixed:

$$R_1 = \frac{\sum_g ||F_g^{exp}| - |F_g^{calc}||}{\sum_g |F_g^{exp}|}, \qquad (2)$$

where F_g^{calc} is the simulated amplitude and F_g^{exp} is the experimental amplitude. The same atom positions and Debye–Waller factors from §2 were used in the simulations, and the

cone semi-angles in the simulations matched the experimental conditions. Thickness was the only parameter that was varied. Values for R_1 for GITO are plotted in Fig. 10. The precession R factor demonstrates a clear global minimum spanning a relatively broad range of thicknesses (consistent with observed thickness fringes in the illuminated particle edge) and the lowest value ($R_1 = 11.97\%$, 121 symmetrized reflections measured) indicates a thickness of 41.5 nm. In comparison, the non-precessed R_1 is much inferior, which does not show a clear minimum (best non-precessed $R_1 = 44.05\%$ at 38 nm, excluding an obviously false minimum at 3.5 nm, 172 reflections). Fig. 11(a) shows experimental precession amplitudes for GITO plotted against calculated amplitudes, demonstrating strong correlation.
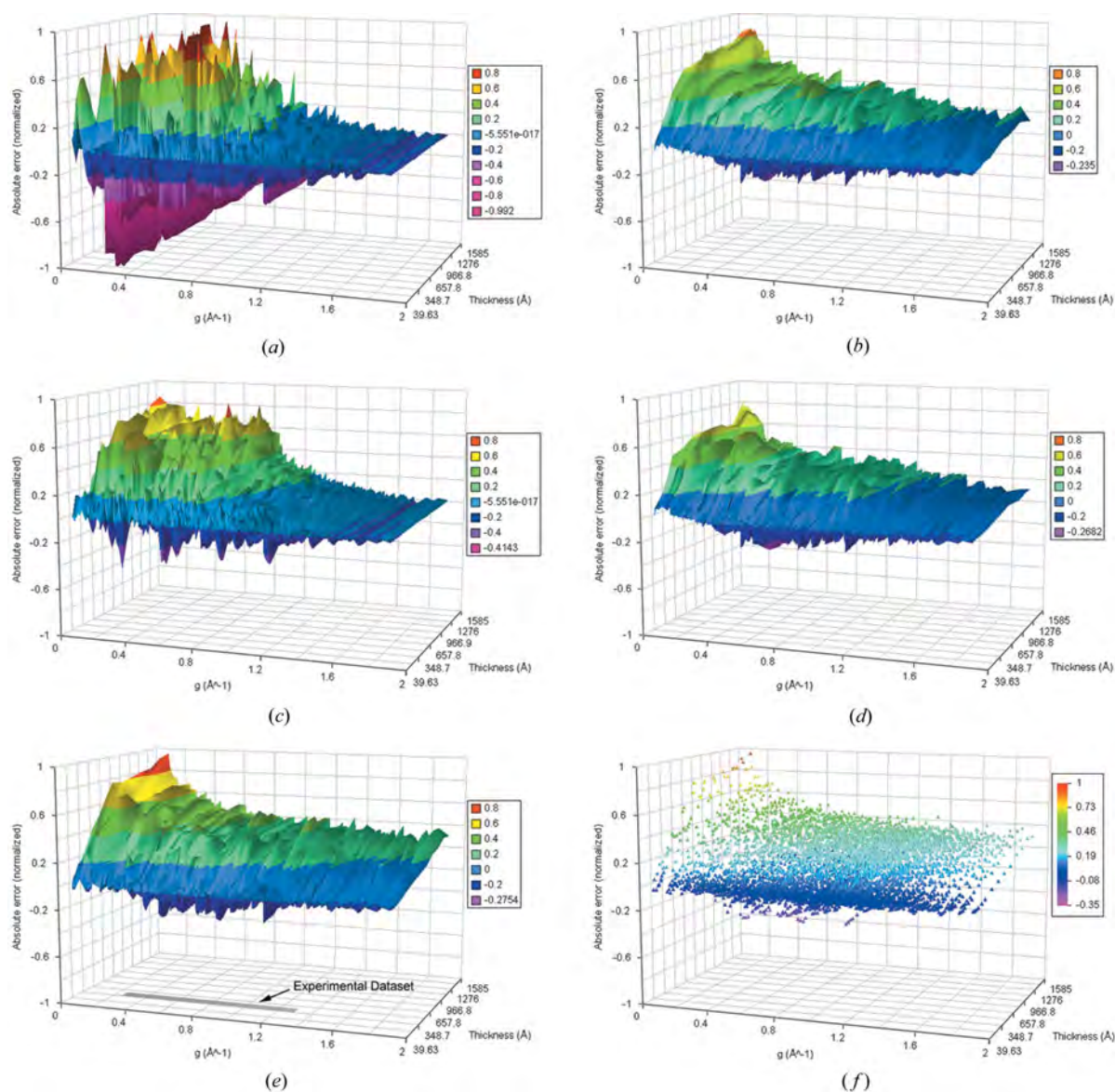

Figure 9
Three-dimensional surface plots of absolute amplitude deviation ($|F_g^{exp}| - |F_g^{kin}|$) against reciprocal-vector magnitude |**g**| and thickness. (a) Dynamical (non-precessed) data-set deviations showing a particularly large spread within the structure-defining reflections $0.25 < |\mathbf{g}|$. (b)–(e) Precession data-set deviations for $\phi = 10, 24, 50$ and 75 mrad tilt angle, respectively. Experimental data-set parameters are shown in plot (c). (f) Scatter plot for 24 mrad showing that for realistic specimen thicknesses (<50 nm) almost all deviations fall within the range $[-0.2, 0.4]$.

This result illustrates a key advantage for both specimen thickness and *ab initio* structure determination: thickness insensitivity. Within the thickness range in Fig. 10 that corresponds to lowest precession R_1 (25–50 nm), non-precessed intensities oscillate rapidly (Fig. 9a) as expected, giving a consistently poor R_1, whereas precessed intensities have much lower frequency of oscillation and are very stable in this range (Fig. 9c). If scattering from constituent thicknesses is very different, wedge-shaped specimens will corrupt intensity ordering (see later). This is clearly seen when comparing simulated and experimental patterns: Figs. 4(a) and (c) (non-precessed) are very dissimilar, whereas Figs. 4(b) and (d) (precessed) show that precession multislice closely matches experiment.

The above analysis was repeated for the MFI system with $\phi = 33$ mrad, resulting in an R factor of $R_1 = 15.26\%$ at a thickness of 127.3 nm [Figs. 5(c) and 11(b)]. Compared with Fig. 10 for GITO, Fig. 5(c) shows even more moderate variation with thickness. The lack of oscillatory behavior here compared with mild oscillations in the GITO case may be related to the larger precession radius used to acquire the MFI pattern (1.67 *versus* 0.96 Å^{-1}). Schematics of the experimental and simulated zone axis for 127.3 nm are compared in Figs. 5(b) and (d), and it can be seen that overall the agreement is quite good considering that no atom positions or thermal factors were adjusted.

4. Discussion

We have attempted herein to give a reasonably detailed analysis of the overall characteristics of precession diffraction, comparing it to the kinematical intensities as one metric. Since it is fairly simple to solve the structure from fully kinematical data using direct methods, some discussion of how well precession data can be treated by direct methods is appropriate.

Conventional direct methods are well established (Schenk, 1992; Giacovazzo, 1998) and have been applied previously with electron diffraction data (Nicolopoulos *et al.*, 1995; Dorset, 1996, 2003a,b; Sinkler, Bengu & Marks, 1998; Gilmore, 1999; Weirich, 2001, 2003; Hovmöller *et al.*, 2002; Dorset *et al.*, 2005). In almost all cases, the effects of dynamical diffraction have either been ignored or taken (often without *a priori* justification) as small. As is well known, even a single atom of a heavy element such as gold at 100 kV is a dynamical scatterer, as is 3 nm of solid hydrogen, and in some cases dynamical diffraction makes the phase problem easier, not harder (*e.g.* Spence, 1998). While there have been multislice calculations of specific cases (Dorset, 1997; Dorset *et al.*, 1999), to date it has only proved possible to make generalizations about the effects of dynamical diffraction on the important terms for direct methods in a few cases (Sinkler, Bengu &
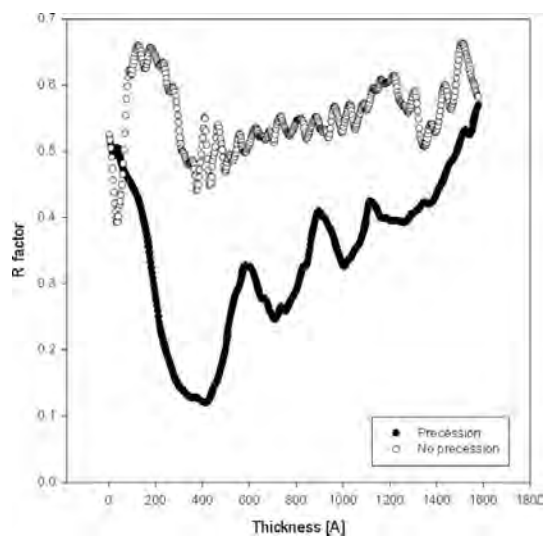
Figure 10
R_1 for the GITO experimental data sets. Precession data sets have a clear global minimum and indicate a nominal thickness of ~41.5 nm. Multislice done at 200 kV with 1000 points; precession data used a 24 mrad cone semi-angle.
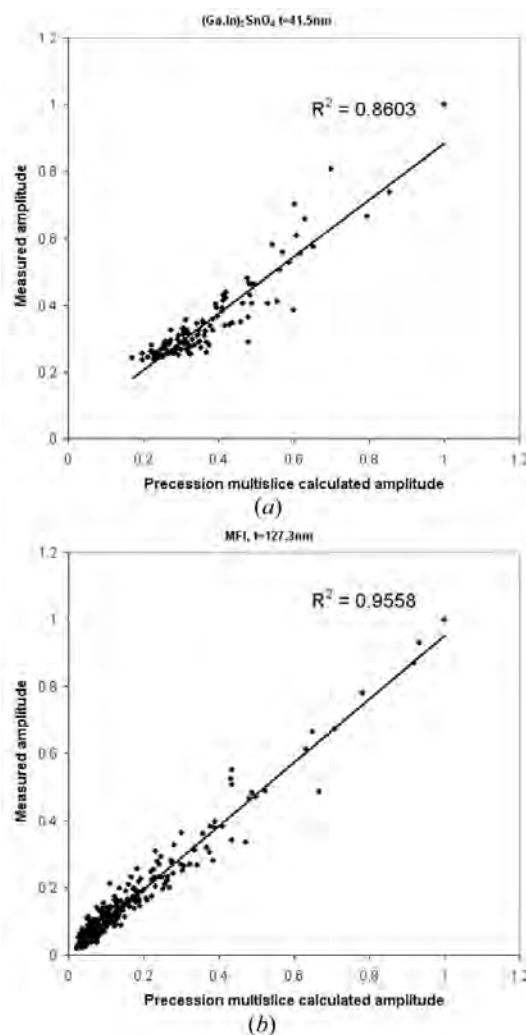
Figure 11
Precession amplitudes (normalized) plotted against amplitudes calculated by precession multislice for (a) GITO and (b) MFI. R^2 is the correlation constant. For comparison, the non-precessed experimental data from GITO (not shown) yielded a much lower correlation constant (~0.23).

Marks, 1998; Sinkler & Marks, 1999b; Hu *et al.*, 2000; Chukhovskii *et al.*, 2001). These can in principle be incorporated into a more general mathematical description of direct methods as a feasible set optimization problem (Marks *et al.*, 1999) to, for instance, recover a complex object *via* a hybrid approach that goes beyond conventional direct methods (Marks & Sinkler, 2003).

The ideal situation is to have as close to kinematical data as possible. This is available from extremely thin specimens (<2 nm) and from surfaces (Marks *et al.*,1998). It is sensible to minimize dynamical effects by using specimens with small to moderate thickness (up to ~20 nm) and atom-like features are usually present in structure maps from very thin specimens. However, problems are common: not only is thickness difficult to control or predict, atom-like features may be at incorrect locations, have the wrong amplitude, or have their amplitude inverted (Babinet solutions). Consequently, considerable work is often required to ascertain the true structure and additional information from characterization techniques other than electron diffraction is often needed.

Some distinct cases exist where conventional direct methods with electron diffraction data can provide relatively easily interpretable information about atomic positions when dynamical diffraction is correctly taken into account (Marks & Sinkler, 2003). The first case is when the scattering is dominated by 1 s channelling states (Lindhard, 1964; Berry, 1971; Gemmell, 1974; Kambe *et al.*, 1974; Tamura & Ohtsuki, 1974; Van Dyck & Op de Beeck, 1996; Sinkler & Marks, 1999a; Geuens & Van Dyck, 2002). While atom-like features can be recovered from such data, the results are difficult to predict for novel structures and to date classical structure completion methods developed for X-ray diffraction in practice often fail with electron diffraction data when the scattering is dominated by 1 s channelling states. A less stringent constraint assumes deviation from kinematical but exploits the fact that the statistical relationships contained within the data set are probably preserved as long as the ranking between the intensity values is preserved (Marks & Sinkler, 2003):

Figure 12
(*a*) The kinematical diffraction pattern of MFI. Encircled regions show systematic rows that are strongly affected by one-dimensional diffraction [see the experimental MFI pattern in Fig. 5(*d*) for comparison]. (*b*) Kinematical diffraction pattern of GITO. The area of the diffraction spots is proportional to their intensity.

$$I_g > I_h \Longleftrightarrow |F_g^{\text{kin}}| > |F_h^{\text{kin}}|, \qquad (3)$$

where I_g is the experimental intensity and F_g^{kin} the kinematical structure factor. This is called 'intensity mapping', and is almost certainly applicable to texture and powder patterns where the combined scattering from multiple crystal orientations can be described by the Blackman formula (Blackman, 1939) and further integrated over thicknesses; it may also be applicable in some other cases.

As the multislice calculations show, precession electron diffraction intensities are not kinematical, and to our knowledge there is no case where they are; dynamical diffraction always occurs. However, it should be clear from the results herein that in many cases intensity mapping is much better in a PED pattern than it is in a conventional diffraction pattern, and improves as the cone semi-angle is increased. One significant caveat is that this is not necessarily true for very low angle reflections near to the transmitted beam. This is simply a geometric effect: for these reflections, the integration over excitation error is much less complete than it is for higher-angle reflections, so the averaging over tilt angles has much less effect. Fortunately, these are not in general what we referred to earlier as the 'structure-defining reflections'. Provided that one uses code that is capable of handling unknown reflections such as EDM (Kilaas *et al.*, 2005), a feasible-set approach (Marks *et al.*, 1998) or maximum entropy (Gilmore, 1999), one can simply remove these from the data set (Own *et al.*, 2006a). An exception to this is the case of large-framework structures for which low-index reflections might be structure-defining. A use of intensities instead of amplitudes is an alternate approach that will focus on the stronger reflections and might produce a reasonable result, particularly in a very thick sample as this is a known limit of the Blackman formula (Blackman, 1939). However, this is really not the right way to 'correct' the data, a topic that we will deal with in more detail in a companion paper (Own *et al.*, 2006b).

One final comment. As mentioned above, precession diffraction is a dynamical process. The ability of an appropriately structured multislice simulation to provide an excellent match to experimental intensities has been shown above, and this demonstrates that dynamical diffraction fully accounts for the data with no additional effects needed. While we do not believe it is appropriate to think about PED as kinematical, there are nevertheless obvious advantages in that it gives intensities which are much closer to kinematical than more conventional diffraction modes. One particular case where the intensities are not going to quickly approximate kinematical is for strong systematic row conditions, a known case where the Blackman formula is lacking (*e.g.* Reimer, 1984; Cowley, 1990). In precession diffraction, the limiting case for a single orientation (large inclination) is going to be a systematic row condition. This clearly shows up in experimental data, for instance in MFI where the kinematical intensity ordering is disrupted along systematic rows [see Fig. 12, with reference to Fig. 5(*d*)]. This is also the reason why kinematically forbidden dynamically allowed spots (glide or
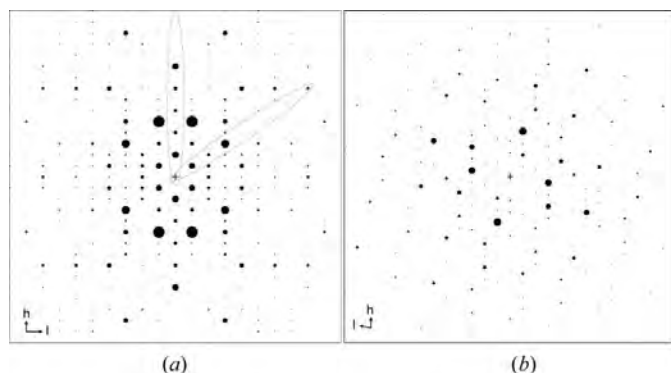
screw axes) are weak to zero in PED. The dynamical routes that lead to their presence involve two-dimensional diffraction which breaks the symmetry. However, in a systematic row condition there is only one-dimensional diffraction, so these spots are weak to forbidden. A proof of this is the Si 222 reflection, which is an accidentally forbidden reflection (*i.e.* not due to any special symmetry conditions) as shown in Vincent & Midgley (1994); the reflection is allowed for a systematic row condition and shows up due to dynamical effects in both normal and precession diffraction modes.

References

Berry, M. V. (1971). *J. Phys.* C**4**, 697–722.

Blackman, M. (1939). *Proc. R. Soc. London Ser. A*, **173**, 68–82.

Cheng, Y. F., Nuchter, W., Mayer, J., Weickenmeier, A. & Gjønnes, J. (1996). *Acta Cryst.* A**52**, 923–936.

Chukhovskii, F. N., Hu, J. J. & Marks, L. D. (2001). *Acta Cryst.* A**57**, 231–239.

Cowley, J. M. (1990). *Diffraction Physics.* Amsterdam: Elsevier.

Dorset, D. L. (1996). *Acta Cryst.* B**52**, 753–769.

Dorset, D. L. (1997). *Acta Cryst.* A**53**, 356–365.

Dorset, D. L. (2003*a*). *Rep. Prog. Phys.* **66**, 305–338.

Dorset, D. L. (2003*b*). *Z. Kristallogr.* **218**, 237–246.

Dorset, D. L., Dumas, P., Cartier, L. & Lotz, B. (1999). *Acta Cryst.* A**55**, 901–907.

Dorset, D. L., Roth, W. J. & Gilmore, C. J. (2005). *Acta Cryst.* A**61**, 516–527.

Edwards, D. D., Mason, T. O., Sinkler, W., Marks, L. D., Poeppelmeier, K. R., Hu, Z. & Jorgensen, J. D. (2000). *J. Solid State Chem.* **150**, 294–304.

Gemmell, D. S. (1974). *Rev. Mod. Phys.* **46**, 129–227.

Gemmi, M., Zou, X. D., Hovmöller, S., Migliori, A., Vennström, M. & Andersson, Y. (2003). *Acta Cryst.* A**59**, 117–126.

Geuens, P. & Van Dyck, D. (2002). *Ultramicroscopy*, **93**, 179–198.

Giacovazzo, C. (1998). *Direct Phasing in Crystallography: Fundamentals and Applications.* New York: Oxford University Press.

Gilmore, C. J. (1999). *Microsc. Res. Tech.* **46**, 117–129.

Gjønnes, J., Hansen, V., Berg, B. S., Runde, P., Cheng, Y. F., Gjønnes, K., Dorset, D. L. & Gilmore, C. J. (1998). *Acta Cryst.* A**54**, 306–319.

Gjønnes, J. & Moodie, A. F. (1965). *Acta Cryst.* **19**, 65–69.

Gjønnes, K., Cheng, Y. F., Berg, B. S. & Hansen, V. (1998). *Acta Cryst.* A**54**, 102–119.

Hovmöller, S., Zou, X. D. & Weirich, T. E. (2002). *Advances in Imaging and Electron Physics*, Vol. 123, pp. 257–289. Amsterdam: Elsevier.

Hu, J. J., Chukhovskii, F. N. & Marks, L. D. (2000). *Acta Cryst.* A**56**, 458–469.

Ishizuka, K. (1982). *Acta Cryst.* A**38**, 773–779.

Kambe, K., Lehmpfuhl, G. & Fujimoto, F. (1974). *Z. Naturforsch. Teil A*, **29**, 1034–1044.

Kilaas, R., Marks, L. D. & Own, C. S. (2005). *Ultramicroscopy*, **102**, 233–237.

Lindhard, J. (1964). *Phys. Lett.* **12**, 126–128.

Ma, Y. & Marks, L. D. (1990). *Acta Cryst.* A**46**, 11–32.

Marks, L. D., Bengu, E., Collazo-Davila, C., Grozea, D., Landree, E., Leslie, C. & Sinkler, W. (1998). *Surf. Rev. Lett.* **5**, 1087–1106.

Marks, L. D. & Sinkler, W. (2003). *Microsc. Microanal.* **9**, 399–410.

Marks, L. D., Sinkler, W. & Landree, E. (1999). *Acta Cryst.* A**55**, 601–612.

Midgley, P. A., Sleight, M. E., Saunders, M. & Vincent, R. (1998). *Ultramicroscopy*, **75**, 61–67.

Nicolopoulos, S., Gonzalezcalbet, J. M., Valletregi, M., Corma, A., Corell, C., Guil, J. M. & Perezpariente, J. (1995). *J. Am. Chem. Soc.* **117**, 8947–8956.

Olson, D. H., Kokotailo, G. T., Lawton, S. L. & Meier, W. M. (1981). *J. Phys. Chem.* **85**, 2238–2243.

Own, C. S., Marks, L. D. & Sinkler, W. (2005). *Rev. Sci. Instrum.* **76**, 033703.

Own, C. S., Sinkler, W. & Marks, L. D. (2006*a*). *Ultramicroscopy*, **106**, 114–122.

Own, C. S., Sinkler, W. & Marks, L. D. (2006*b*). In preparation.

Own, C. S., Subramanian, A. K. & Marks, L. D. (2004). *Microsc. Microanal.* **10**, 396–396.

Reimer, L. (1984). *Transmission Electron Microscopy*. Berlin: Springer.

Saxton, W. O., Pitt, T. J. & Horner, M. (1979). *Ultramicroscopy*, **4**, 343–353.

Schenk, H. (1992). *Direct Methods of Solving Crystal Structures*. Dordrecht: Springer.

Sinkler, W., Bengu, E. & Marks, L. D. (1998). *Acta Cryst.* A**54**, 591–605.

Sinkler, W. & Marks, L. D. (1999*a*). *J. Microsc.* **194**, 112–123.

Sinkler, W. & Marks, L. D. (1999*b*). *Ultramicroscopy*, **75**, 251–268.

Sinkler, W., Marks, L. D., Edwards, D. D., Mason, T. O., Poeppelmeier, K. R., Hu, Z. & Jorgensen, J. D. (1998). *J. Solid State Chem.* **136**, 145–149.

Spence, J. C. H. (1998). *Acta Cryst.* A**54**, 7–18.

Tamura, A. & Ohtsuki, Y. H. (1974). *Phys. Status Solidi*, **62**, 477–480.

Van Dyck, D. & Op de Beeck, M. (1996). *Ultramicroscopy*, **64**, 99–107.

Vincent, R. & Midgley, P. A. (1994). *Ultramicroscopy*, **53**, 271–282.

Weirich, T. E. (2001). *Acta Cryst.* A**57**, 183–191.

Weirich, T. E. (2003). *Z. Kristallogr.* **218**, 269–278.

Weirich, T. E., Portillo, J., Cox, G., Hibst, H. & Nicolopoulos, S. (2006). *Ultramicroscopy*, **106**, 164–175.

Xu, P., Jayaram, G. & Marks, L. D. (1994). *Ultramicroscopy*, **53**, 15–18.